Title

Topological controls on the dissolution kinetics of glassy aluminosilicates.

Journal

Journal of the American Ceramic Society, 100(12)

ISSN

0002-7820

Authors

Oey, Tandré
Kumar, Aditya
Pignatelli, Isabella
et al.

Publication Date

2017

DOI

10.1111/jace.15122

Peer reviewed

Published in final edited form as:
J Am Ceram Soc. 2017 ; 100(12): . doi:10.1111/jace.15122.

Topological controls on the dissolution kinetics of glassy aluminosilicates

Tandré Oey[a,*], **Aditya Kumar**[a], **Isabella Pignatelli**[a], **Yingtian Yu**[b], **Narayanan Neithalath**[c], **Jeffrey W. Bullard**[d], **Mathieu Bauchy**[b], **Gaurav Sant**[a,e]

[a]Laboratory for the Chemistry of Construction Materials (LC^2), Department of Civil and Environmental Engineering, University of California, Los Angeles, CA 90095, USA

[b]Physics of Amorphous and Inorganic Solids Lab (PARISlab), Department of Civil and Environmental Engineering, University of California, Los Angeles, CA 90095, USA

[c]School of Sustainable Engineering and the Built-Environment, Arizona State University, Tempe, AZ 85287, USA

[d]Engineering Laboratory, National Institute of Standards and Technology, Gaithersburg, MD 20899, USA

[e]California NanoSystems Institute, University of California, Los Angeles, CA 90095, USA

Abstract

Fly ash which encompasses a mixture of glassy and crystalline aluminosilicates is an abundant supplementary cementitious material (SCM), valuable for replacing ordinary portland cement (OPC) in the binder fraction in concrete. Because higher OPC replacement levels are desired, it is critically important to better understand and quantify fly ash reactivity. By combining molecular dynamics (MD) simulations and vertical scanning interferometry (VSI), this study establishes that the reactivity of the glassy fractions in a fly ash with water (i.e., their aqueous dissolution rate) is controlled by the number of constraints placed on atoms within the disordered aluminosilicate network. More precisely, an Arrhenius-like dependence of dissolution rates on the atomic network topology is observed. Such *topological controls* on fly ash reactivity are highlighted for a range of U.S. commercial fly ashes spanning CaO-enriched and SiO_2-enriched compositions. The structure-property relationships reported herein establish an improved framework to control and estimate fly ash-cement interactions in concrete.

Keywords

Fly ash; glass; reactivity; topological constraint theory; dissolution

1.0. Introduction

At current levels of global production, the manufacture of ordinary portland cement (OPC) is responsible for nearly 9% of anthropogenic CO_2 emissions [1]. To mitigate the impacts

*Corresponding author: G. Sant, gsant@ucla.edu.

of such CO_2 emissions, it is common to replace OPC with supplementary cementitious materials (SCMs) such as fly ash in the binder fraction in concrete, a process commonly known as "dilution" [2,3]. Substantial efforts have been made to characterize fly ash compositions, and their potential impacts on the engineering properties of cementitious formulations [4–6], but far fewer studies have attempted to establish the origins of, and to quantify fly ash reactivity [7–12]. Establishing the origin of and controls on fly ash reactivity is prerequisite knowledge, needed to rank different fly ashes in terms of their suitability as an OPC replacement agent [13]. Towards this end, we provide new insights into the atomistic origins of fly ash reactivity so as to place its use, on an informed scientific basis. The outcomes of this work are applicable not only to fly ash, but more generally to other amorphous/glassy SCM's including slags, clays, and natural pozzolans.

2.0. Materials and methods

Seven commercially available fly ashes were chosen to encompass representative yet abundant U.S. fly ashes (and coal streams) with a range of glassy compositions. This includes three Class C ("CaO-enriched") fly ashes, and four Class F ("SiO_2-enriched") fly ashes, as classified by ASTM C618 [14]. The fly ash compositions are detailed below (see Tables 1–2). The bulk oxide composition of each fly ash was determined using X-ray fluorescence as per ASTM D4326 [14] (XRF, Table 1). To establish the fly ash mineralogy, quantitative X-ray diffraction (QXRD, Table 2) analyses were carried out on powdered fly ash samples, using ZnO (about 20 mass %) as an internal standard. The samples were mounted in metallic (zero-background) holders, and the surface gently textured to minimize preferred orientation errors. A Bruker D8 Advance diffractometer in a θ-θ configuration using Cu-Kα radiation (λ = 1.54 Å) was used to scan the powder samples on a rotating stage between 5° and 70° (2θ) in continuous mode with a six second step time. X-ray structure information for relevant anhydrous and hydrated crystalline phases was sourced from the literature or standard databases to provision a custom *control-file* for Rietveld refinement that was carried out using TOPAS©.

The *average* dissolution rate of each fly ash was measured at (25 ± 3 °C, i.e., based on the maximum temperature variation over a 24 hours period) using vertical scanning interferometry (VSI) [15]. By directly tracking the evolution of the surface topography with time, VSI accesses the true dissolution rate of a dissolving solid [15–18]. The technique features significant advantages over methodologies that are based on analysis of solution compositions because it is unaffected by complexities including: 1) inaccurate knowledge of the solid's surface area, or the presence of particles that are distributed over a wide size-range [18], 2) metastable barrier formation that may be relevant to glassy systems [19], 3) incongruent dissolution [20], and/or 4) ion adsorption on dissolving or reacting surfaces [21–23].

The dissolution rates were quantified using a so-called raindrop procedure[f] [15], by which the solution's pH and composition remain essentially constant over the course of the

[f]It should be noted that in the rain-drop procedure, while the "bulk" undersaturation of the solution with respect to the dissolving solids will change negligibly, the reduction in undersaturation of the solution may be more substantial in close proximity (i.e., within the first 10 nm) of the solid surface. While this may result in undersaturation gradients within a "static" water-drop; i.e., close-to,

experiment. The typical l/s (liquid-to-solid mass ratio) used was on the order of 50,000 for a contact time of approximately 5 min per raindrop cycle for a minimum of 15 cycles. The solvent was evacuated using a compressed N_2 stream between raindrop cycles. Solution pH values[g] of 10, 12, 13, and 14.3 were achieved using reagent grade sodium hydroxide (NaOH), dissolved in 18 MΩ ("MilliQ") water.

Since the dissolution studies were carried out on technical fly ashes, i.e., those containing both glassy and crystalline compounds (see Table 2), data collection was initiated after the first 15 minutes of "contact time" (dissolution period). This was necessary to permit dissolution and exhaustion of the fast dissolving crystalline compounds such as C_3A whose dissolution, if it were to occur simultaneously, may have interfered with observations of dissolution of the glassy compounds. It should be noted that the dissolution of compounds such as quartz, which is often present in the highest abundance amongst crystalline compounds (e.g., see Table 2), is not a concern as quartz dissolves three orders of magnitude more slowly than the glassy phases present in fly ash [16], and hence will not impact the results.

The average composition of each ash's glassy components was established by subtracting the XRD-based compositions of crystalline compounds from the XRF-based total (simple) oxide compositions.

The structure of the glassy phase, assumed homogeneous[h], was then assessed via molecular dynamics (MD) simulations. Due to the limited availability of realistic inter-atomic potentials (that can encompass any combination of elements), the compositions of the simulated systems were restricted to the following oxides: SiO_2 and Al_2O_3 (network forming species), and CaO, MgO, Na_2O, K_2O (network modifying species), while maintaining the molar ratios among these oxides as equivalent to the native fly ashes. The glasses were created using the conventional quenching method at zero pressure in the *NPT* ensemble as follows: (1) heating the system at 4000 K to lose the memory of its initial configuration, (2) cooling to 300 K at a cooling rate of 1 K/ps, (3) relaxing the structure at 300 K for an additional 100 ps, and (4) equilibrating the structure for an additional 100 ps in the *NVT* ensemble for statistical averaging [26]. The simulations were performed with a timestep of 1 fs using the interatomic potential parametrized by Teter [27]. This potential has been extensively studied and has been shown to predict realistic glass structures [28–30]. The simulations agree broadly with previous simulations studies [26,31] on three main points. First, Si is four-fold coordinated by oxygen atoms. Second, alkali and alkaline-earth cations tend depolymerize the network by forming non-bridging oxygen (NBO) species.

and further away from the dissolving solid surface. While artifacts of this nature are indeed unavoidable, they are expected to be more important for solids that dissolve under transport control (i.e., when the rate of transport of ions away from the particle surface is rate-controlling; i.e., for faster dissolving solids) than interface control (i.e., when the transport of ions is not rate limiting in dissolution; i.e., for slower dissolving solids such as silicates).

[g]Solution pH values have been verified by experiments measuring the extent of carbonation (via pH) over time. Over the duration of experiments conducted herein, no appreciable carbonation (within error) was observed.

[h]It is well known that the glassy phase of fly ash is not homogenous. This assumption excludes any effects which may arise from a heterogeneous mixture of glassy and crystalline phases as is present in fly ash. However, the glass is assumed homogeneous because (a) it has been shown that an average homogeneous glass provides an accurate representation of the physical response of fly ash materials during dissolution occurring during cement hydration[10], and (b) such an assumption is necessary to facilitate characterization of fly ash in a manner which is both feasible and relevant (i.e. characterization which may be conducted on an as-received fly ash, and reflect said ash's behavior).

Third, Al is four- or (rarely) five-fold coordinated and tends to repolymerize the network by consuming the NBOs, or by creating three-fold “tri-cluster” oxygen (TO) species.

The structure of the simulated glasses is analyzed within the framework of topological constraint theory (TCT) [32,33]. TCT captures the relevant features of the atomic topology which have an important influence on the kinetics of dissolution [16], while filtering out less relevant structural details. This is achieved by simplifying complex atomic networks into simple mechanical trusses, wherein the nodes (the atoms) are connected to each other through constraints (i.e., the chemical bonds): the radial bond-stretching (BS) and angular bond-bending (BB) constraints. Rather than relying on unproven guesses regarding the connectivity of the atoms, the total number of constraints per atom (n_c) was directly determined from the MD simulations by following an established methodology [31,34], wherein the radial and angular excursions of the neighbors of each atom are computed to enumerate the BS and BB constraints, respectively.

In agreement with previous studies [31,34], the following observations are made: (1) Si atoms create four BS constraints with the neighboring O atoms and five BB constraints (to define the tetrahedral environment); (2) Al atoms create four or five BS constraints, but do not possess any BB constraints; (3) alkali and alkaline-earth species create a composition-dependent number of BS constraints with the surrounding NBOs, but do not show any BB constraints; and (4) bridging oxygen (BO) atoms form one BB constraint (three in the case of TOs). Finally, in accordance with previous observations [16], charge-compensating alkali or alkaline-earth cations (i.e., those in the vicinity of Al, which do not create any NBOs) are excluded from this enumeration as they do not contribute to the rigidity of the network.

3.0. Results and discussion

Figure 1(a) shows the measured dissolution rates of all the different fly ashes as a function of the solution pH. As expected, the dissolution rate increases with pH because greater hydroxyl concentrations (activities) facilitate hydrolysis of silicate networks [35]. Surface speciation induced by the presence of sodium (i.e., from NaOH which exchanges with the protons of terminal silanol groups [22]) may somewhat enhance fly ash dissolution rates [22], but this effect should be relatively constant across all fly ash compositions because it is related solely to the concentration of added sodium. In the high pH range used in this study, the dominant driving force for dissolution arises from the elevated activity of $[OH]^-$ ions, which induces nucleophilic attack of tetrahedral $[SiO_4]^{4-}$ or $[AlO_4]^{5-}$ units present in the glassy compounds in fly ashes [36]. It should be noted that while changes to the coordination state of network forming $[SiO_4]^{4-}$ or $[AlO_4]^{5-}$ units may indeed impact dissolution rates, in the present case, the MD simulations show that for these fly ash materials, the average coordination number of silicon and aluminum shows little deviation from the expected value of 4 ± 0.03 – as a result, the dissolution rates do not show any dependence on atomic coordination. The plot also shows that the dissolution rates of the lower-calcium Class F fly ashes (F1 through F4) are lower than those of the higher-calcium C ashes (C1 through C3) across the entire range of caustic pH’s considered.

Figure 1(b) shows that the measured dissolution rate of all the fly ashes in this study decreases exponentially with the number of constraints, n_c, for a given pH. The same behavior was observed recently for a range of silicate-solids by Pignatelli et al. [16]. Indeed, for a given pH the dissolution rates of all fly ashes lie along the same line. It should be noted that decreases in dissolution rate generally correspond to lower concentrations of calcium in the fly ash, but this is not true in all cases. For example, fly ashes F2 and F3 both have lower CaO content and greater dissolution rates than F1, as shown in Figure 1(a). This strongly suggests that the predominant C and F classifications of fly ashes as established by ASTM C618 are insufficient to predict or rank a fly ash's relative reactivity. Rather, a "network ratio" parameter, as demonstrated by Oey et al. [13], or the number of topological constraints per atom as shown in this study, are more reliable indicators of ash reactivity. Apart from the ASTM C618 based "C or F" classification of fly ash, the glass science community has often expressed the properties of glasses in terms of their degree of depolymerization, NBO/T, which represents the number of non-bridging oxygens per tetrahedral unit [13,37]. However, Pignatelli et al. have recently shown that even NBO/T is not always reliable indicator of glass dissolution behavior [16].

The dissolution rate is shown to be correlated to the rigidity (n_c) of the whole network, including the alkali and alkaline-earth cations, rather than the rigidity of only the aluminosilicate "skeleton" network. This suggests that while dissolution kinetics are dominated (rate-limited) by the rate of breakage of the higher energy Si/Al–O bonds, the rate of breakage of the lower energy bonds that are created due to the presence of the network modifiers is also relevant; albeit to a smaller extent. This is in agreement with the observations of Boolchand et al. who noted that glass hardness was correlated with the rigidity of the overall network, including the contributions of modifier atoms [39]. A significant observation in Figure 1(b) is that, in spite of being composed of a myriad of glassy compounds of disparate compositions, the "average" dissolution rate of the glassy fly ash solids, and the associated number of atomic constraints, reliably represent fly ash behavior. As remarked earlier, this observation supports the work of Oey et al., who formulated a network ratio parameter to demonstrate that relative fly ash reactivities can be ranked based on knowledge of their average glassy compositions [11,13,40].

When the fly ash dissolution rates shown in Figure 1(b) are plotted along with additional dissolution rate data for glassy silica, quartz, and several aluminosilicate glasses including albite, jadeite, nepheline and sodium silicate glass (denoted as "Natural" glass; see Figure 1c [16,36,38]) – the exponential dependence of dissolution rate on n_c is preserved[i]. Significantly, the regression of these data using an exponential function of the form $K = K_0 \exp(-n_c E_0/RT)$ reveals that the averaged, or apparent, activation energy needed to break a unit atomic constraint is $E_0 \approx 23.9$ kJ/mol. This assessment of E_0 for heterogeneous fly ash glasses that are produced during an uncontrolled, complex quenching process is similar to that observed for stoichiometric and fully-compensated aluminosilicate glasses and pure

[i]To reiterate, the assumption that the glass in fly ash consists of a single homogeneous phase is at the root of poor quality of this exponential dependence among the seven fly ashes. Interferences from either (a) uniquely reactive or unreactive glasses from among the heterogeneous distribution present, and/or (b) uniquely reactive or unreactive crystalline phases may both result in higher or lower dissolution rates (measured on the bulk fly ash, not the isolated glass) than those predicted by number of atomic constraints calculated for an assumed homogeneous glass.

silicate solids (E_0 = 25.5 kJ/mol [16]). In support of the commentary above, the small difference in magnitudes suggests that the constraint rupture energy is largely controlled by the network formers (e.g., $[SiO_4]^{4-}$ and/or $[AlO_4]^{5-}$ species); albeit with smaller but relevant contributions that arise from the presence and distributions of modifier atoms whose influences merit further study. This indicates that, to a first approximation, fly ash dissolution rates are primarily dictated by the activation energy for bond rupture amongst $[SiO_4]^{4-}$ or $[AlO_4]^{5-}$ units [36]; wherein the activation energy is described as $E_a = n_c E_0$ [16]. This dependence of dissolution rates on the number of atomic constraints is shared by other rate processes in glasses, including ion diffusion and conduction, and suggests that the three typical mechanisms involved in glass dissolution, namely hydration, hydrolysis, and ion exchange, can be formalized within a consistent thermodynamic framework which encompasses the material's atomic architecture/topology [16].

4.0. Summary and conclusions

Across a wide range of commercially available fly ashes, the dissolution rates of the glassy constituents are shown to depend on the number of atomic constraints placed on a given atom in the glass network. This constraint dependence of dissolution rates is described by an Arrhenius-like expression that permits determination of the average energy needed to rupture a unit atomic constraint. This rupture energy is on the order of 25 kJ/mole across a range of silicate solids including fully compensated and highly modified glasses, as well as pure silicates (i.e., glassy silica and quartz). Such a dependence of dissolution rates on the number of constraints suggests that rate processes including dissolution, diffusion, and ion conduction all are similarly predicated on the topology of the atomic network. This allows for rationalizing rate phenomena such as dissolution within a consistent thermodynamic framework based on the energy required for bond rupture. This framework also enables a robust way to measure, analyze, and rank fly ash reaction rates as a function of their average glassy compound composition and the atomic topology of the glassy compounds in fly ash. Such understanding is needed to better inform and enhance the use of fly ash as a supplementary cementitious material (SCM) without sacrificing concrete performance.

Acknowledgements

The authors acknowledge financial support for this research by COMAX, a joint UCLA-NIST consortium that is supported by its industrial and government agency partners, the U.S. Department of Transportation (U.S. DOT) through the Federal Highway Administration (DTFH61-13-H-00011) and National Science Foundation (CAREER Award: 1235269). This research was conducted in: Laboratory for the Chemistry of Construction Materials (LC^2) and Laboratory for the Physics of AmoRphous and Inorganic Solids (PARISlab) at UCLA and the Engineering Laboratory at NIST. The authors gratefully acknowledge the support that has made these laboratories and their operations possible. The contents of this paper reflect the views and opinions of the authors, who are responsible for the accuracy of the datasets presented herein, and do not reflect the views and/or policies of the funding agencies, nor do the contents constitute a specification, standard or regulation.

References

[1]. Miller SA, Horvath A, Monteiro PJ Readily Implementable Techniques Can Cut Annual CO2 Emissions from the Production of Concrete by Over 20%. Environ. Res. Lett. 2016; 11(7): 74029.

[2]. Malhotra VM Fly ash, Slag, Silica Fume, and Rice-Husk Ash in Concrete: A Review. Concr. Int. 1993; 15(4): 23–28.

[3]. Rivera F, Martínez P, Castro J, et al. Massive Volume Fly-Ash Concrete: A More Sustainable Material with Fly Ash Replacing Cement and Aggregates. Cem. Concr. Compos. 2015; 62: 104–112.

[4]. Mehta PK Influence of Fly Ash Characteristics on the Strength of Portland-Fly Ash Mixtures. Cem. Concr. Res. 1985; 15: 669–674.

[5]. Papadakis VG Effect of Fly Ash on Portland Cement Systems: Part I. Low-Calcium Fly Ash. Cem. Concr. Res. 1999; 29: 1727–1736.

[6]. Papadakis VG Effect of Fly Ash on Portland Cement Systems: Part II. High-Calcium Fly Ash. Cem. Concr. Res. 2000; 30: 1647–1654.

[7]. Roy DM, Luke K, Diamond S. Characterization of Fly Ash and its Reactions in Concrete. MRS Online Proceedings Library Archive. 1984; 43: 3.

[8]. Aughenbaugh KL, Chancey RT, Stutzman P, et al. An Examination of the Reactivity of Fly Ash in Cementitious Pore Solutions. Mater. Struct. 2013; 46: 869–880.

[9]. Snellings R. Surface Chemistry of Calcium Aluminosilicate Glasses. J. Am. Ceram. Soc. 2015; 98: 303–314.

[10]. Hu Q, Aboustait M, Ley MT, et al. Combined Three-Dimensional Structure and Chemistry Imaging with Nanoscale Resolution. Acta Mater. 2014; 77: 173–182.

[11]. Hu Q, Ley MT, Davis J, et al. 3D Chemical Segmentation of Fly Ash Particles with X-ray Computed Tomography and Electron Probe Microanalysis," Fuel, 2014; 116: 229–236.

[12]. Brouwers HJH, Van Eijk RJ Fly Ash Reactivity: Extension and Application of a Shrinking Core Model and Thermodynamic Approach. J. Mater. Sci. 2002; 37: 2129–2141.

[13]. Oey T, Huang C, Worley R, et al. Linking Fly Ash Composition to Performance in Cementitious Systems. World of Coal Ash Proceedings. Nashville, TN, May 5-7, 2015.

[14]. ASTM Standards Website. Available at: http://www.astm.org/Standards/. Accessed on 3/9/2015 at 3:03 p.m. PST.

[15]. Kumar A, Reed J, Sant G. Vertical Scanning Interferometry: A New Method to Measure the Dissolution Dynamics of Cementitious Minerals. J. Am. Ceram. Soc. 2013; 96: 2766–2778.

[16]. Pignatelli I, Kumar A, Bauchy M, et al. Topological Control on Silicates' Dissolution Kinetics. Langmuir. 2016; 32: 4434–4439. [PubMed: 27108867]

[17]. Pignatelli I, Kumar A, Shah K, et al. Vertical Scanning Interferometry: A New Method to Quantify Re-/De-Mineralization Dynamics of Dental Enamel. Dent. Mater. 2016; 32(10): e251–e261. [PubMed: 27520495]

[18]. Pignatelli I, Kumar A, Alizadeh R, et al. A Dissolution-Precipitation Mechanism is at the Origin of Concrete Creep in Moist Environments. J. Chem. Phys. 2016; 145: 54701.

[19]. Hellmann R, Cotte S, Cadel E, et al. Nanometre-Scale Evidence for Interfacial Dissolution–Reprecipitation Control of Silicate Glass Corrosion. Nat. Mater. 2015; 14: 307–311. [PubMed: 25559424]

[20]. Cailleteau C, Devreux F, Spalla O, et al. Why Do Certain Glasses with a High Dissolution Rate Undergo a Low Degree of Corrosion? J. Phys. Chem. C. 2011; 114: 5846–5855.

[21]. Bennett PC, Melcer ME, Siegel DI, et al. The Dissolution of Quartz in Dilute Aqueous Solutions of Organic Acids at 25 C. Geochim. Cosmochim. Acta. 1988; 52: 1521–1530.

[22]. Dove PM, Crerar DA Kinetics of Quartz Dissolution in Electrolyte Solutions Using a Hydrothermal Mixed Flow Reactor. Geochim. Cosmochim. Acta. 1990; 54: 955–969.

[23]. Myers RJ, Geng G, Li J, et al. The Role of Adsorption Phenomena in Cubic Tricalcium Aluminate Dissolution. Langmuir. 2016; 33(1): 45–55. [PubMed: 27977205]

[24]. Le Saoût G, Kocaba V, Scrivener K. Application of the Rietveld Method to the Analysis of Anhydrous Cement. Cem. Concr. Res. 2011; 41: 133–148.

[25]. Winburn RS, Grier DG, McCarthy GJ, et al. Rietveld Quantitative X-ray Diffraction Analysis of NIST Fly Ash Standard Reference Materials. Powder Diffr. 2000; 15: 163–172.

[26]. Bauchy M. Structural, Vibrational, and Elastic Properties of a Calcium Aluminosilicate Glass from Molecular Dynamics Simulations: The Role of the Potential. J. Chem. Phys. 2014; 141(2): 024507. [PubMed: 25028027]

[27]. Du J, Cormack AN The Medium Range Structure of Sodium Silicate Glasses: a Molecular Dynamics Simulation. J. Non-Cryst. Solids. 2004; 349: 66–79.

[28]. Cormack AN, Du J. Molecular Dynamics Simulations of Soda–Lime–Silicate Glasses. J. Non-Cryst. Solids. 2001; 293: 283–289.

[29]. Du J, Corrales LR Compositional Dependence of the First Sharp Diffraction Peaks in Alkali Silicate Glasses: A Molecular Dynamics Study. J. Non-Cryst. Solids. 2006; 352: 3255–3269.

[30]. Wang B, Yu Y, Lee YJ, et al. Intrinsic Nano-Ductility of Glasses: The Critical Role of Composition. Front. Mater. 2015; 2: 11.

[31]. Bauchy M, Micoulaut M. Atomic Scale Foundation of Temperature-Dependent Bonding Constraints in Network Glasses and Liquids. J. Non-Cryst. Solids. 2011; 357: 2530–2537.

[32]. Phillips JC, Topology of Covalent Non-Crystalline Solids I: Short-Range Order in Chalcogenide Alloys. J. Non-Cryst. Solids. 1979; 34: 153–181.

[33]. Mauro JC, Topological Constraint Theory of Glass. Am. Ceram. Soc. Bull. 2011; 90: 31.

[34]. Bauchy M, Abdolhosseini Qomi MJ, Bichara C, et al. Nanoscale Structure of Cement: Viewpoint of Rigidity Theory. J. Phys. Chem. C. 2014; 118: 12485–12493.

[35]. Maraghechi H, Rajabipour F, Pantano CG, et al. Effect of Calcium on Dissolution and Precipitation Reactions of Amorphous Silica at High Alkalinity. Cem. Concr. Res. 2016; 87: 1–13.

[36]. Hamilton JP Corrosion Behavior of Sodium Aluminosilicate Glasses and Crystals. The Pennsylvania State University, 1999.

[37]. Shelby JE, Introduction to Glass Science and Technology. Royal Society of Chemistry, Cambridge CB4 0WF, UK. 2005.

[38]. Hamilton JP, Brantley SL, Pantano CG, et al. Dissolution of Nepheline, Jadeite and Albite Glasses: Toward Better Models for Aluminosilicate Dissolution. Geochim. Cosmochim. Acta. 2001; 65: 3683–3702.

[39]. Boolchand P, Zhang M, Goodman B. Influence of One-Fold-Coordinated Atoms on Mechanical Properties of Covalent Networks. Phys. Rev. B. 1996; 53: 11488.

[40]. Chancey RT Characterization of Crystalline and Amorphous Phases and Respective Reactivities in a Class F Fly Ash. The University of Texas at Austin, 2008.

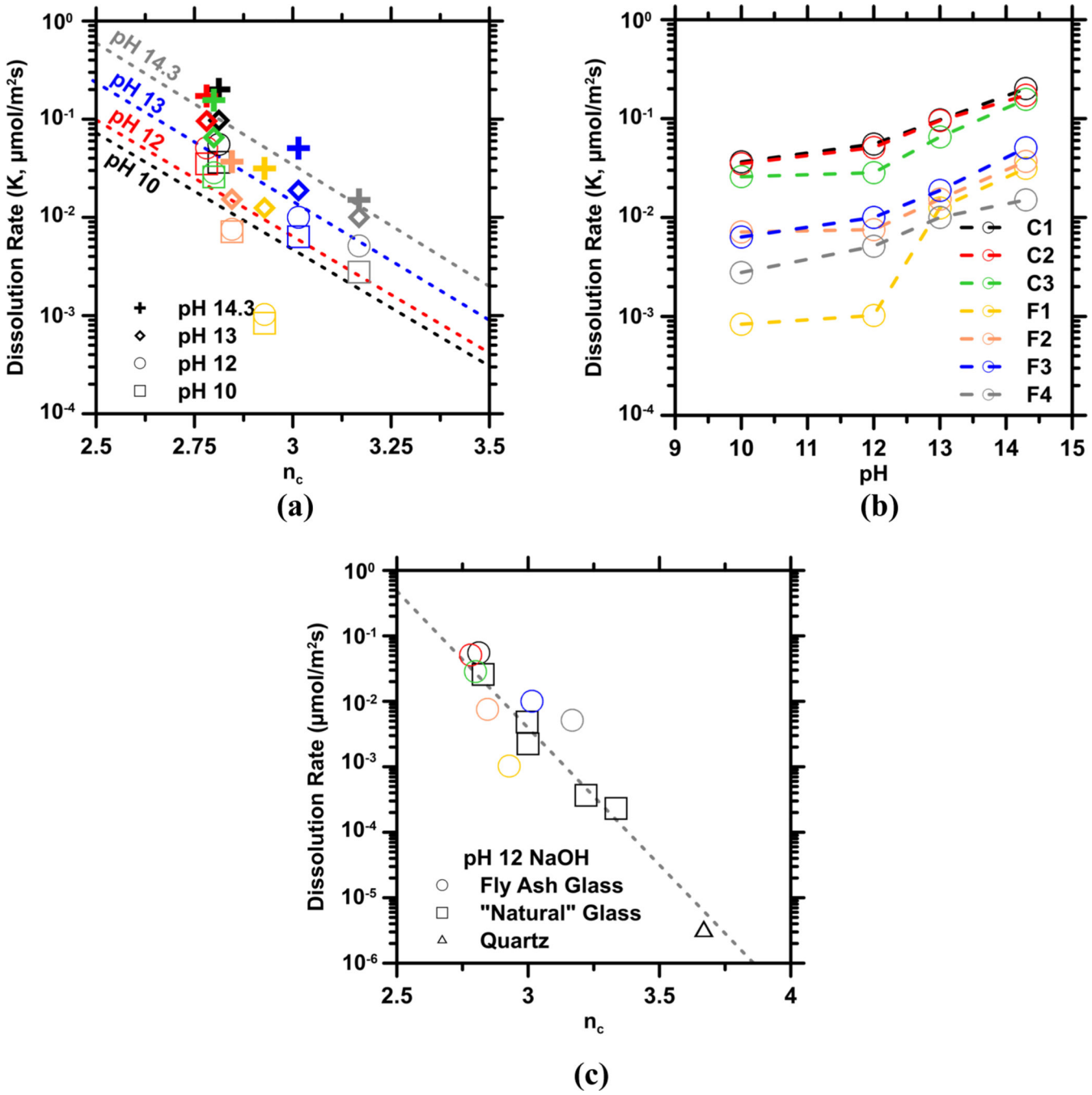

Figure 1:

The dissolution rates of the seven fly ashes as a function of: (a) solution pH, and (b, c) the number of constraints per atom (n_c, unitless) calculated by MD simulations. For consistent comparison between solids of different compositions, the dissolution rates are expressed as moles of O_2 dissolved per m^2 of surface area per second. The data in (b, c) is fitted using exponential functions. The color of datapoints in (b) correspond to the legend presented in (a) to indicate which fly ash each point represents, while the symbol shape corresponds to the solution pH, with squares, circles, diamonds, and crosses representing pH 10, 12, 13,

and 14 respectively. The data in (c) includes dissolution rates for silica and quartz, as well as glassy equivalents of albite, jadeite, nepheline, and sodium silicate glass (see [16,36,38]). The exponential functions represent an Arrhenius-like expression of the form: $K = K_0 \exp(-n_C E_0 / k_B T)$, where: K is the dissolution rate in μmol/m^2•s, K_0 is the intrinsic dissolution rate constant in μmol/m^2•s, E_0 is the energy required to break a unit atomic constraint (E_0 = 23.9 kJ/mole in Figure 1c), k_B is Boltzmann's constant in kJ/mol•K, and T is the thermodynamic temperature in degrees K.

Table 1:

The simple oxide compositions of fly ashes measured by X-ray fluorescence (mass %). Standard deviations given in the last column indicate typical values listed for the technique [24].

	Class C			Class F				σ [24]
	C1	**C2**	**C3**	**F1**	**F2**	**F3**	**F4**	**(±)**
SiO_2	35.44	36.08	40.08	50.75	53.97	60.48	57.98	0.40
Al_2O_3	17.40	18.03	20.44	15.77	20.45	22.85	27.71	0.20
Fe_2O_3	7.15	6.02	6.29	6.28	5.62	4.47	6.35	0.10
SO_3	2.34	2.91	1.62	0.79	0.52	0.46	0.25	0.10
CaO	26.45	25.90	21.35	15.05	12.71	5.20	1.64	0.40
Na_2O	1.90	1.86	1.46	3.29	0.57	2.14	0.50	0.03
MgO	5.73	5.24	4.56	4.57	2.84	1.19	1.07	0.10
K_2O	0.53	0.46	0.71	2.14	1.11	1.31	2.69	0.04
P_2O_5	0.95	1.03	1.23	0.24	0.30	0.14	0.17	0.01
TiO_2	1.19	1.34	1.42	0.61	1.29	1.16	1.38	0.01
Total	99.08	98.87	99.16	99.49	99.38	99.40	99.74	

Table 2:

Relative abundance of crystalline compounds of the fly ashes measured by quantitative X-ray diffraction and Rietveld refinement (mass %), and the corresponding standard errors [25].

	Class C			Class F				σ [25]
	C1	**C2**	**C3**	**F1**	**F2**	**F3**	**F4**	**(%)**
Quartz	10.06	11.10	9.81	6.83	16.64	16.48	14.15	10
Mullite	0.86	0.90	1.14	–	5.08	10.17	20.01	10
Anhydrite	2.80	1.84	1.01	1.61	0.97	–	–	15
Lime	1.16	1.04	0.33	–	–	–	–	15
Periclase	3.81	2.17	2.50	1.70	0.30	0.19	–	20
Magnetite	1.66	2.36	1.64	2.08	1.76	2.03	1.96	15
Merwinite	6.98	4.19	3.98	3.66	–	–	–	25
Calcio-Olivine	0.43	1.34	1.57	–	–	–	–	–
Ilmenite	–	–	–	0.58	–	–	–	–
β-C_2S	4.50	6.30	5.75	–	–	–	–	1.4
C_2AS	4.45	3.27	3.76	–	–	–	–	–
C_3A (cubic)	5.90	5.06	6.14	–	–	–	–	25
C_3A (orthorhombic)	2.13	2.73	2.90	–	–	–	–	25
Amorphous/Glassy	55.25	57.69	59.47	83.53	75.25	71.13	63.87	2
Total	100	100	100	100	100	100	100	